LipiGo: A Versatile DNA-Lipid Nanoparticle Hybrid for Precision Drug Delivery

Karoline Kadletz*, Ceren Kimna*, Valentin Kenneth Reichenbach, Olga Carofiglio, Denise Jeridi, Sofia Hu, Igor Khalin, Jakub Grzejdak, Ying Chen, Izabela Horvath, David-Paul Minde, Mayar Ali, Taras Sych, Luciano Höher, Eren Aydeniz, Yagmur Ayse Kulcu, Alessio Ricci, Arthur Liesz, Erdinc Sezgin, Siegfried Ussar, Farida Hellal, Markus Elsner, Ali Ertürk

Abstract: Lipid nanoparticles (LNPs) are established carriers for nucleic acid delivery, however, achieving efficient delivery to non-hepatic tissues remains a major challenge. Here, we present LipiGo, a nanocarrier platform engineered by integrating short single stranded DNA molecules into the lipid nanoparticle structure. Using whole body tissue clearing, advanced imaging and AI-based analysis, we show that LipiGo redirects functional mRNA delivery to lymphoid organs, particularly the spleen. Immune cell profiling further reveals enhanced uptake within key immune populations, including antigen-presenting cells, compared to standard LNPs. Beyond passive redistribution, LipiGo leverages DNA hybridization to enable modular attachment of targeting ligands for active targeting as demonstrated by cell-specific delivery to white adipocytes. Overall, the dual-purpose design principle of LipiGo demonstrates high modularity and efficiency, enabling tissue and cell specific delivery beyond hepatic applications.

1. Introduction

Nucleic acid therapeutics offer opportunities for both prophylactic and therapeutic applications with the potential to address targets previously considered undruggable by conventional methods. Their broad clinical translation, however, remains constrained by targeted delivery.

Lipid nanoparticles (LNPs) represent one of the most clinically advanced vehicles for the delivery of nucleic acids as they combine high loading capacity, stability in circulation, and low toxicity. Their impact has become evident in approved medicines, including SARS-CoV-2 vaccines and a therapy for hereditary transthyretin-mediated amyloidosis, with numerous additional candidates currently in clinical trials.

Despite their advantages, intravenously administered LNPs intrinsically accumulate in the liver, which limits their utility in extrahepatic tissues and increases the risk of liver-related toxicity[1,2]. Although alternative administration routes can shift biodistribution toward different organs, precise delivery beyond the liver requires rational strategies to control nanoparticle tropism, which remains one of the central challenges in the field.

Efforts to achieve organ-, tissue-, and cell type-specific delivery with LNPs can be broadly categorized into passive and active strategies[3]. Varying lipid ratios, introducing lipids with distinct chemistries or expanding the number of constituent lipids reshapes the biomolecular corona that forms around LNPs upon exposure to biofluids, and thereby passively modulates interactions with immune receptors, cells, and tissues[4]. Active strategies, in contrast, involve decorating the particle surface with targeting ligands such as antibodies or aptamers[5,6]. Ligands are most commonly attached to LNPs via PEG-lipids, which protrude from the LNP surface[7]. However, PEG-lipids are designed to rapidly shed upon administration to facilitate cellular internalization and endosomal escape[8]. As PEG shedding typically occurs within minutes of administration, together with the strong intrinsic hepatic tropism of LNPs, efficient engagement of targeting ligands with their cognate receptors is often limited[9]. Thus, cell type-specific targeting following systemic delivery with active strategies has not been achieved *in vivo*[10]. Achieving sub-organ level specificity beyond the liver, therefore, requires overcoming dominant hepatic accumulation while simultaneously leveraging active targeting via surface-displayed ligands, highlighting the need for a vehicle design that integrates both passive and active targeting mechanisms.

Here, we introduce LipiGo, a lipid-based hybrid nanoparticles generated by partially substituting cholesterol with cholesterol-modified single-stranded DNA (ssDNA) that protrude from the particle surface. In this base formulation, the DNA strands alter particle physicochemical properties and redirect functional mRNA delivery from the liver toward immune organs. Beyond this intrinsic retargeting, the protruding DNA strands also serve as modular handles for ligand hybridization, thereby combining passive and active targeting in a single design and enabling cell-specific delivery, as demonstrated with a white adipocyte–targeting DNA aptamer.

2. Results and Discussion

Design and characterization of LipiGo nanoparticles

To generate LipiGo, we partially substituted the cholesterol component in standard lipid nanoparticle formulations with a 26-base single stranded DNA (ssDNA) modified with a cholesterol moiety at the 3' end. This modification results in nanoparticles with ssDNA protruding from their surface (**Fig. 1a,b**).

While generating the base LipiGo formulation, lipid ratios were adapted from Cheng *et al.*[11] for efficient mRNA encapsulation and release. Particles were assembled by mixing an aqueous phase containing EGFP-encoding, fluorescently labeled mRNA with an ethanol phase containing DLin-MC3-DMA (23.8 mol %), PEG2000-C-DMG (4.3 mol %), DSPC (23.8 mol %), DMG-PEG(2000) (0.5 mol %), and cholesterol (47.6 mol %), with partial substitution of cholesterol by cholesterol-modified ssDNA at varying degrees.

Compared to conventional LNPs, LipiGo displayed altered physicochemical properties. Their hydrodynamic size increased slightly from ~50 nm to ~68 nm (**Fig. 1c**). Increasing the degree of cholesterol-ssDNA substitution from 20 to 50 % shifted the zeta potential towards more negative values (-8.2 ± 3 mV and -10.7 ± 7 for 20 % and 50 % LipiGo, respectively) (**Fig. 1d**). A similar change in zeta potential was observed across different DNA sequences and ionizable lipid chemistries (*i.e.*, ALC-1315 and SM1502), indicating that the effect is sequence and lipid chemistry independent (**Fig. S1a**). Across formulations, the polydispersity index (PDI) remained below 0.2 for all variants, indicating narrow and monomodal size distributions and RNA encapsulation efficiency was not significantly affected by addition of the DNA-cholesterol (**Fig. 1e**). Importantly, particles remain stable for at least 24 h in serum-supplemented media (**Fig. 1f**). Together, these results indicate that while preserving uniformity, stability and loading capacity, cholesterol-ssDNA protrusions provide a tunable parameter on nanoparticle features to alter physicochemical characteristics, *i.e.*, size and zeta potential, which are known to influence the interactions with biological material, affecting their biodistribution[4].

Beyond tuning physical characteristics, the surface-exposed DNA handles of LipiGo provide modular sites for ligand attachment through complementary base pairing. To demonstrate this versatility, we conjugated two structurally distinct ligands, *i.e.*, an immunoglobulin G (IgG) antibody and a short DNA aptamer AS1411. The IgG antibody was first conjugated to a complementary DNA strand *via* maleimide chemistry, followed by hybridization to the LipiGo handle (**Fig. 1a**). The aptamer was extended with a short region complementary to the LipiGo handle strand and therefore could be directly hybridized to the handle DNA. Both ligand-conjugated LipiGo variants retained comparable physicochemical properties within an acceptable size range (**Fig. 1g,h**). Successful aptamer hybridization was confirmed by an increase in double-stranded DNA content together with a decrease in zeta potential (**Fig. S1c**). Importantly, this DNA-mediated conjugation strategy not only ensures controlled orientation and display of targeting ligands but also avoids the altered biodistribution and enhanced toxicity associated with complement activation, a phenomenon recently reported for nanoparticles functionalized with targeting antibodies using conventional chemistries such as dibenzocyclooctyne-mediated coupling[12].

We next assessed the cellular compatibility and intracellular behavior of LipiGo *in vitro*. LipiGo particles did not induce detectable cytotoxicity within the tested concentration range (1-10 µg mRNA per mouse) as measured by cell viability assay in HEK cells (**Fig. S2a**). To evaluate endosomal escape and cytoplasmic delivery, we employed the Gal8 recruitment assay in HeLa cells, which are stably expressing Galectin8-mRuby3 fusion protein[13]. Upon endosomal membrane rupture, Gal8-mRuby3 binds to the inner lumen of the disrupted endosomes resulting in punctate fluorescent spots, indicating cytosolic release of the particle remnants and their cargo. We observed a significantly increased endosomal rupture at 4 h after LipiGo treatment compared to the standard LNPs (**Fig. 1i,j**). By 24 h, Gal-8 positive puncta in LipiGo treated cells decreased to levels comparable with those observed with standard LNPs, suggesting that LipiGo promotes more rapid endosomal escape. Consistent with this, cells incubated with LipiGo showed stronger fluorescent mRNA signal at 24 h relative to standard LNPs (**Fig. 1k**), indicating enhanced cytoplasmic retention and reduced intracellular degradation. These results suggest that LipiGo interacts differently with endosomal membranes or trafficking pathways, leading to more efficient release of its cargo. Since limited endosomal escape remains a key bottleneck in mRNA delivery, the accelerated endosomal rupture and sustained cytoplasmic mRNA signal with LipiGo highlights its potential to overcome this challenge.

Following in vitro evaluations, we next evaluated the half-life of LipiGo particles in bloodstream using in vivo two-photon microscopy. LipiGo exhibited a circulation half-life of ~120 minutes, which was slightly shorter than that of the parent LNPs, suggesting faster tissue uptake. This finding is consistent with the enhanced cellular uptake observed *in vitro*, and fall falls within the range reported for other LNP formulations assessed with alternative techniques[14] (**Fig. 1l-n**).

LipiGo exhibits enhanced biodistribution to lymphatic tissues

To evaluate the *in vivo* biodistribution of LipiGo nanoparticles, we intravenously injected 1 µg mRNA/mouse (0.067 mg/kg mRNA) and analyzed particle distribution after 1 h using our in-house developed "Single Cell Precision Nanocarrier Identification (SCP Nano)" pipeline[15]. SCP Nano integrates whole-body tissue clearing of LNP/LipiGo administered mice, light sheet fluorescence microscopy (LSFM) imaging, and deep learning-based signal quantification at single cell-resolution for biodistribution mapping (**Fig. 2a**). As expected, intravenous administration of standard LNPs led to predominant hepatic accumulation, limiting their ability to effectively target other organs[2]. Using high resolution whole-body imaging, we observed LipiGo and LNP signals in other major organs including the spleen, lungs, and heart (**Fig. 2b**, **Fig. S3**). Some of these organ-specific signals would be difficult to capture using conventional techniques such as bioluminescence imaging (**Fig. S4b**).

Interestingly, LipiGo particles exhibited a pronounced tropism for lymphoid and immune associated organs, particularly in the spleen and lymph nodes, which are targeted less by conventional LNPs following intravenous administration (**Fig. 2b,c**). Standard LNPs and LipiGo particles also show differences in their intra-organ distribution (**Fig. 2c**). For example, liver distribution patterns for LipiGo particles were found to be more homogeneous and dispersed than for standard LNPs, which showed perivascular clustering. These differences likely reflect deeper tissue penetration associated with faster

133 blood clearance as indicated by the lower signal at 60 minutes in the blood that was measured with
134 intravitreal microscopy (**Fig. 1l-n**).

135 To test whether the observed shift in biodistribution was independent on the specific LNP formulation,
136 we generated LipiGo particles using other clinically validated ionizable lipids, i.e., ALC-0315 (used in
137 BioNTech's COVID-19 vaccine) and SM-102 (used in Moderna's Covid 19 vaccine). Physicochemical
138 properties were similar across all LipiGo variants (**Fig. S1a**). Notably, incorporation of the DNA-lipid
139 handle into the base formulation consistently led to a more uniform biodistribution pattern in the liver
140 and to a substantial shift in tropism towards immune organs (**Fig. 2d, Fig. S3a**), supporting the
141 compositional flexibility of the LipiGo platform.

142 We next evaluated whether sequence-level engineering of the DNA handle further modulates the
143 biodistribution. We designed a DNA handle variant containing a CpG motif known to activate immune
144 cells via Toll-like receptor (TLR9) [16-18]. While the original LipiGo sequence was designed to be
145 biologically inert, both sequences were identical in length and total GC content to control for structural
146 effects. LipiGo particles formulated with the CpG-containing sequence (LipiGo-CpG), exhibited similar
147 hydrodynamic size and zeta potential, ruling out colloidal effects on biological behavior (**Fig. S1b**).
148 Following the SCP Nano pipeline, we found that LipiGo-CpG showed even stronger spleen tropism
149 compared to the LipiGo with non-functional DNA handles, (**Fig. S3e**). These findings demonstrate that
150 oligonucleotide sequence alone can be leveraged to tune targeting. Together, the findings demonstrate
151 the modularity of LipiGo across different ionizable lipid backbones in maintaining immune organ
152 targeting, as well as its tunability through DNA handle sequence level to further refine biodistribution,
153 highlighting its flexibility for organ tropism.

154 **Quantitative organ and cell type profiling reveals LipiGo-mediated immune tropism despite**
155 **residual hepatic distribution**

156 Having qualitatively assessed particle distribution, we next performed deep-learning based
157 quantification of organ-level targeting using automated segmentation of organs and mRNA signal (**Fig.**
158 **3a**). Based on whole-body images, we anticipated the major difference of LipiGo particles to be their
159 reduced hepatic accumulation and increased localization to lymphatic organs (**Fig. 2a,b**). However,
160 unbiased organ-by-organ quantification revealed interesting, yet, unexpected, findings. Even though
161 the preferential accumulation of LipiGo in the spleen was validated, the visually perceived reduction in
162 liver targeting was not supported quantitatively (**Fig. 3b**). Compared to LNPs, LipiGo particles exhibited
163 slightly reduced lung accumulation, consistent with previous reports showing that LNPs formulated with
164 cationic lipids preferentially localize to the lung whereas the more negatively charged formulations
165 demonstrate spleen tropism[4]. Across all formulations, minimal particle accumulation was quantified in
166 the brain, heart, and kidneys, and no significant differences were detected among LipiGo variants with
167 varying degrees of DNA handle modification (**Fig. 3b**).

168 Revisiting the raw images for a closer inspection provided insight into these observations. In LipiGo-
169 injected mice, the mRNA signal in the livers appeared more sparsely distributed, whereas in standard

170 LNP-injected mice, the signal was concentrated in focal regions as distinct patches near blood vessels.
171 This perivascular clustering likely contributed to the apparent overestimation of liver enrichment by
172 visual inspection alone, underscoring the importance of unbiased quantification. The more dispersed
173 distribution pattern observed with LipiGo may reflect differences in particle kinetics. As shown in the
174 circulation half-life experiments (**Fig. 1l-n**), fewer LipiGo particles remained in bloodstream at 60
175 minutes, suggesting more rapid tissue uptake. It is possible that, by the time of sacrifice, *i.e.*, 60 minutes
176 post injection, LipiGo particles potentially penetrated deeper into liver parenchyma, leading to a more
177 homogeneous and less visually prominent signal compared to the vascular-concentrated standard
178 LNPs. This integrated view, together with the image-based quantification and kinetic data highlights the
179 value of multimodal analysis in revealing subtle but biologically meaningful differences in nanocarrier
180 behavior.

181 In addition, we generated liver and spleen biodistribution density maps to facilitate direct comparison of
182 accumulation patterns between standard LNP and LipiGo formulations in terms of liver to spleen
183 tropism. These density heat maps further illustrated these differences, with LipiGo-injected animals
184 showing fewer high-density patches in the liver and stronger accumulation in the spleen (**Fig. 3c**). The
185 enhanced spleen targeting of LipiGo was consistently validated by SCP-nano, as demonstrated both in
186 the representative heat maps (**Fig. 3c**) and in corresponding quantitative dot counts at the organ level
187 (**Fig. 3b**).

188 With LipiGo showing a strong tropism for lymphoid organs, we next investigated the immune cell types
189 targeted across key immune-relevant tissues including blood, lymph nodes, spleen, and liver. Flow
190 cytometric profiling of 20 distinct immune cell subsets revealed a clear shift in cellular tropism compared
191 to standard LNPs (**Fig. 3d, Fig. S5**). Notably, LipiGo demonstrated enhanced uptake across several
192 immune cell types, particularly in secondary lymphoid organs. In the spleen, LipiGo increased the
193 percentage of mRNA homing immune cells from 26.51% to 65.16% with the most prominent
194 contributions from antigen presenting cells such as $CD35^+$ follicular dendritic cells (5.8-fold), $F4/80^+$
195 macrophages (11.3-fold), and $CD11c^+$ dendritic cells (2.4-fold) (**Fig. 3d,e**). T-cell delivery also improved
196 with higher frequencies of both CD4+ and CD8+ subsets labeled in the spleen and lymph nodes, despite
197 overall lower levels. High targeting rates of both the antigen presenting and effector cells at these critical
198 sites suggests a potential utility of LipiGo particles to trigger and shape specific immune responses.
199 Furthermore, beyond adaptive immunity, LipiGo broadened innate immune engagement with elevated
200 signals observed in $Ly6C^+$ monocytes and $Ly6G^+$ neutrophils across peripheral organs. By contrast,
201 standard LNPs showed substantially lower mRNA delivery to these immune subsets in the spleen, and
202 remained largely confined to liver-resident cells. Notably, even within the liver, LipiGo outperformed
203 standard LNPs for most immune cell subtypes, with strong increases in targeting efficiency in $CD4^+$ T
204 cells and $Ly6C^+$ monocytes and $Ly6G^+$ neutrophils. Together, these results highlight the potential of
205 LipiGo to engage both innate and adaptive immune cells within immunologically active tissues.

206 **Functional delivery of mRNA to the immune cells with reduced hepatic expression**

207 Having demonstrated through whole body mRNA cargo imaging that LipiGo enhances tropism to
208 lymphatic organs, we next investigated whether these particles enable functional delivery, *i.e.*,
209 successful cytoplasmic mRNA release and translation to protein. Mice were injected intravenously with
210 LipiGo particles carrying EGFP mRNA (0.067 mg/kg) and sacrificed 48 h later. EGFP expression was
211 detected with nanobody staining using the nanoDISCO whole body clearing method [15].

212 In contrast to the biodistribution data, functionality readout revealed significantly reduced EGFP
213 expression in LipiGo-administered mouse livers (**Fig. 4a,b, Fig. S4a**). Moreover, we observed different
214 protein expression distribution pattern within the liver compared to standard LNPs. While LNPs induced
215 concentrated, perivascular clusters of EGFP, LipiGo-treated livers exhibited minimal and more diffuse
216 signal (**Fig. 4b**). By contrast, LipiGo still induced robust EGFP expression in lymphoid tissues, with
217 spleen expression markedly surpassing that of LNPs. In addition to the spleen, higher EGFP-signals
218 are also seen in thymus and in the lymph nodes when the mRNA is delivered with LipiGo rather than
219 with standard LNPs. Thus, although LipiGo distributes systemically, efficient mRNA translation is
220 selectively enriched in immune organs.

221 To validate this organ tropism with an orthogonal readout, we performed bioluminescence imaging by
222 loading nanoparticles with FLuc mRNA (0.067 mg/kg). Quantitative analysis of signal in the spleens
223 and livers confirmed the enhanced expression in the spleen and confirmed the functional liver
224 detargeting effect in LipiGo-treated animals (**Fig. 4c, Fig. S4b**).

225 To resolve the expression at the cellular level, we carried out immunofluorescence staining of fresh
226 frozen tissue sections from the livers and spleens (**Fig. 4d-f**). Consistent with whole-body imaging,
227 standard LNPs induced strong EGFP expression in the liver, whereas LipiGo-treated livers showed
228 minimal signal. In the spleen, however, LipiGo exhibited robust and broadly distributed protein
229 expression (**Fig. 4f**). Notably, unlike the clustered expression patterns seen in standard LNP-treated
230 livers, LipiGo-mediated expression appeared more diffuse and less concentrated. Immunostaining
231 confirmed that LipiGo particles were internalized to greater extent by $CD45^+$ immune cells as compared
232 to standard LNPs, and resulted in slightly elevated number of cells received functional delivery in these
233 populations (**Fig. S4c**). These findings again confirm the flow cytometry results, providing a direct
234 functional readout of protein expression in immune cell subsets.
235

236 **LipiGo elicits minimal systemic response and forms a Angpt1-rich protein corona**

237 Having established functional delivery of mRNA to immune tissues, we next evaluated the in vivo safety
238 profile of LipiGo by assessing systemic cytokine responses and serum protein composition. Cytokine
239 levels were profiled 48 h post-injection (0.168 mg mRNA/kg mouse) using a 13-plex flow-cytometry
240 based immunoassay.
241 Except for IL-1α, cytokine concretions remained below the technical limit of quantification for both
242 standard LNPs and LipiGo, suggesting that no major systemic inflammatory response was triggered
243 (**Fig. S2b**). Key inflammatory mediators commonly associated with acute nanocarrier toxicity, including
244 IL-6, TNF- α, and IFN- γ were undetectable in both groups. Notably, the absence of IL-6 induction is

245 particularly relevant given the presence of ssDNA on the LipiGo surface, which could potentially engage
246 TRL9 (**Fig. S2b**).
247 Next, we measured markers for metabolic stress and liver toxicity in mouse serum after 1h of
248 LNP/LipiGo circulation, injecting a high dose of 0.67 mg mRNA/kg mouse (**Fig. S2c**). LipiGo and LipiGo-
249 CpG showed a modest but non-significant increase in glucose and lactate compared to standard LNPs
250 and untreated controls, hinting to a general inflammatory response reaction after the injection of the
251 particles. However, since the cytokine panel 48h after injection does not show adverse effects, the
252 inflammatory response seems to be small and of short duration. All liver stress and damage markers
253 (AST, ALT, KETONE) were similar to the negative control for all particles - indicating that neither of the
254 particles causes hepatotoxicity (**Fig. S2c**). Together, these findings demonstrate that LipiGo maintains
255 a favorable safety profile, with minimal systemic immune activation and no signs of acute toxicity, even
256 at elevated doses.
257
258 Upon exposure to biological fluids, nanoparticles rapidly adsorb a layer of biomolecules primarily
259 composed of proteins on their surface, forming a biomolecular corona that critically influences their
260 colloidal stability, biodistribution, and organ tropism[19-22]. To determine whether an altered corona
261 composition contributes to the distinct tropism of LipiGo particles, we performed comparative proteomic
262 profiling of the protein coronas formed on LipiGo and standard LNPs using LC-MS/MS (**Fig. S6a**).
263 Principal component analysis (PCA) revealed clear separation between the protein corona profiles of
264 LipiGo and standard LNPs, independent of CpG-rich motif inclusion, suggesting that the DNA-handle
265 modification consistently alters protein adsorption patterns (**Fig. S6b**).
266 Interestingly, among the differentially enriched proteins, Angiopoietin-1 (Angpt1) was consistently and
267 significantly enriched in all LipiGo coronas independent of the ionizable lipid used in formulation (**Fig.
268 S6c**). The consistent enrichment of Angpt1 in the LipiGo protein corona may contribute to enhanced
269 immune organ targeting by promoting interactions with Tie2-expressing endothelial cells abundant in
270 lymphatic tissues, including lymph nodes and spleen[23]. These interactions could facilitate nanoparticle
271 retention or uptake within these organs. Moreover, Angpt1 is known to regulate endothelial cell stability
272 and vascular permeability. Its significant enrichment on the nanoparticle surface could modulate
273 endothelial barrier properties, potentially enabling more efficient nanoparticle extravasation from the
274 bloodstream into tissues and explaining the faster blood clearance and more tissue distribution of LipiGo
275 that we observed. These combined effects, *i.e.*, enhanced receptor mediated interactions and altered
276 vascular permeability may contribute to the observed redistribution of LipiGo nanoparticles toward
277 lymphatic organs and the faster and deeper tissue penetration.
278
279 **Aptamer functionalization of LipiGo enables cell specific targeting *in vitro* and *in vivo***
280 So far we showed that the integration of ssDNA into an LNP formulation passively altered their *in vivo*
281 fate. However, beyond changing the physicochemical characteristics, these DNA strands also provide
282 a versatile platform for active ligand attachment *via* DNA hybridization, enabling straightforward
283 conjugation of diverse targeting ligands including antibodies or their fragments, peptides, and DNA/RNA
284 aptamers.

To demonstrate the utility of DNA handles for active targeting, we functionalized LipiGo particles with DNA-based aptamers by hybridization to complementary DNA handles pre-incorporated in the formulation (**Fig 1a**). Upon aptamer hybridization, we observed a remarkable shift towards a more negative zeta potential (**Fig. S1c**). Although minor non-specific adsorption was detected on control LNPs lacking the DNA handle, the pronounced changes in these physicochemical properties confirmed specific and efficient aptamer conjugation.

First, we evaluated the targeting performance of aptamer-functionalized LipiGo *in vitro* using differentiated white and brown adipocytes. For these experiments, we selected a novel DNA aptamer AS1 specifically targeting the Asc-1 protein[24], which is highly expressed on white adipocytes but not on brown adipocytes.

Confocal microscopy revealed substantial internalization of AS1-LipiGo particles carrying fluorescently labeled mRNA into the cytoplasm of white adipocytes in an incubation period of 40 minutes (**Fig. 5a**). Cargo mRNA was localized as clusters within intracellular compartments, suggesting endosomal trafficking. In contrast, untargeted LipiGo particles and control LNPs incubated with free AS1 aptamers exhibited only weak, non-specific surface association with negligible cellular uptake (**Fig. 5b**, upper panel). To confirm cell type specificity, the same formulations were incubated with brown adipocytes lacking the target surface protein. As expected, all formulations including the targeting AS1-LipiGo, showed minimal cellular uptake (**Fig. 5b**, lower panel). These results collectively demonstrate that active functionalization of LipiGo particles enables the specific internalization of mRNA into target cells.

Having confirmed specific uptake *in vitro*, we next evaluated whether the active targeting strategy translates to tissue-specific delivery *in vivo*. Whole body clearing and imaging revealed very strong accumulation of AS1-LipiGo in the white adipocyte fat tissue (WAT) close to the injection site (**Fig. 5f**). Next, to assessed the functional delivery. AS1-LipiGo particles encapsulating luciferase-encoding mRNA were administered subcutaneously into mice. Live animal bioluminescence imaging (**Fig. S7a**) and subsequent *ex vivo* analysis of harvested organs 24 h post-injection revealed highly localized and robust luciferase expression predominantly within the white adipose tissue proximal to the injection site (inguinal WAT) (**Fig. S7b**). Importantly, this expression was significantly higher compared to that from untargeted LipiGo controls, indicating the tissue target specificity of AS1-LipiGo particles. While minimal off-target expression was detected in the liver, spleen, and kidneys, the expression in distal WAT depots (*e.g.*, interscapular) was also negligible (**Fig. 5g**). This biodistribution profile suggests that either most of the particles were readily taken up by the inguinal WAT already before reaching other parts of the body, or that biodistribution throughout the body takes longer than 24 h when administered subcutaneously. In conclusion, these findings demonstrate that the LipiGo platform enables the modular attachment of functional aptamers for cell-specific delivery and expression of mRNA cargo *in vitro* and *in vivo*, establishing a promising and versatile approach for targeted nanomedicine.

Conclusions

The ability to direct nucleic acid nanocarriers to specific organs, tissues and cell types is a central step towards expanding their therapeutic utility. In this study, we demonstrate LipiGo as a flexible platform that combines passive and active ligand-mediated targeting within a single nanocarrier design, By embedding DNA handles into the LNP framework, LipiGo combines altered characteristics driving redistribution from the liver to lymphoid organs with modular functionalization through DNA hybridization. This dual strategy expands the therapeutic reach of LNPs well beyond hepatic applications. LipiGo enabled selective and functional mRNA delivery to immune cell-rich organs while reducing hepatic expression, and further demonstrated utility as active targeting nanocarrier, achieving receptor specific delivery to white adipocytes *in vitro* and *in vivo*. The ability to unite systemic detargeting, lymphoid tropism and customizable ligand attachment highlights LipiGo as a programmable nanocarrier platform. This modular strategy could enable rapid customization of nanocarriers across diverse therapeutic areas - providing a blueprint for programmable drug delivery systems. Future studies will be directed at translating LipiGo-based constructs into therapeutic applications.

339 **Methods**

340

341 **LNP/LipiGo preparation**

342 LNPs/LipiGo particles were prepared using the ethanol dilution method. All lipids with specified molar
343 ratios (Dlin-MC3-DMA/DSPC/cholesterol/PEG-DMG at 47.6:23.8:23.8:4.8 %) were dissolved in ethanol
344 absolute (<99.8%), and mRNA was dissolved in 50 mM acetate buffer (pH 4.0). Those two solutions
345 were mixed at an aqueous-to-ethanol volume ratio of 3:1 to a final N:P ratio of 6 and then incubated for
346 10 min at room temperature. The final LNP formulations were dialyzed (MWCO 3.5 kDa) against sterile
347 filtered PBS for 1 h per 100 ul LNP volume to remove the ethanol and neutralize the pH. Standard
348 LNPs were formulated using the molar ratios above. For LipiGo particles, a certain molar percentage
349 (10%, 20% or 50%) of the cholesterol was subsidized with cholesterol bound ssDNA (26nt long) and
350 included in the lipid phase before formulation, the particles were then dialyzed with dialysis tubes with
351 a MWCO of 12kDa.

352

353 **Physicochemical characterizations of LNP/LipiGo particles**

354 **DLS and Zeta potential measurements**

355 The hydrodynamic diameter, polydispersity index (PDI) and zeta potential of the LNPs were measured
356 by DLS (Malvern Zetasizer Pro). For measuring the size, the particle solution was diluted 1:50 with
357 sterile filtered PBS and for measuring the zeta potential particles were diluted with nuclease free water.
358 Plots were generated with GraphPad Prism and show the mean size (nm) of triplicates ± SD.

359 **Attachment of targeting ligands to LipiGo particles**

360 Attachment of aptamers: Aptamers with a bridge complementary to the ssDNA protruding from the
361 LipiGo particles was folded by heating at 95°C for 5 min and then cooling down on ice until further use.
362 LipiGo particles and aptamers were mixed at a molar ratio of 1:1 (binding sites on particles: aptamer)
363 in PBS and then hybridized on a temperature ramp in a thermocycler at 37°C-20°C, -1°C per minute.
364 Unbound aptamers (30 kDa) were removed using 50 kDa Amicon filters (Sigma-Aldich, UFC505008),
365 that were pre-wetted with 0.1M PBS and then filled with the LipiGo-aptamer product and spun down at
366 8000 rcf for 10 minutes. 3 PBS wash steps followed, each for 5 min at 8000rcf, before inverting the filter
367 into a new collection tube and spinning down the purified product

368 Attachment of protein-based ligands: Protein based ligands, such as antibodies, were attached to the
369 thiolated complementary ssDNA strand of the LipiGo anchored handle. First, antibodies were
370 functionalized with maleimide groups using SMCC chemistry as described in the reference[25]. Briefly,
371 antibodies were dissolved in PBS (pH 7.2) and reacted with a 20-fold molar excess of Sulfo-SMCC
372 (A39268, Thermo Fisher Scientific), dissolved in DMSO (final DMSO with antibody <10% v/v), for 30 min
373 at room temperature. The activated antibody was purified using desalting columns (PD Spintrap-25,
374 GE28-9180-04, Sigma-Aldrich) into PBS containing 1 mM EDTA. Separately, thiol-modified
375 oligonucleotides were reduced by incubation with a 100-fold molar excess of TCEP (T2556,
376 ThermoFisher Scientific) for 20 min at room temperature. Excess TCEP was removed by ethanol
377 precipitation at −80 °C. For conjugation, reduced oligo-SH was added to maleimide-activated antibody
378 at a 10:1 molar ratio (oligo:antibody), and the mixture was incubated overnight at 4 °C. Final conjugates

379 were purified using 50 kDa molecular weight cut-off centrifugal filters (Amicon Ultra) to remove unbound
380 oligo.
381 The antibody-oligonucleotide product was then hybridized to the LipiGo platform the same way as the
382 aptamer as described above.
383 **Single particle profile (SPP) analysis of particles containing mRNA**
384 SPP measurements were carried out as described by Sych et al.[26] To measure the number of particles
385 carrying mRNA cargo, cargo and lipid shell had to be labeled in different fluorescent wavelengths.
386 Particle cargo (mRNA) was labeled with AF-647 and the lipid particle core was labeled with Fast-
387 DiO(D3898, Invitrogen). Single Particle Profiling was performed using the setup for confocal acquisition
388 („spot scan") at a Zeiss LSM 780 microscope. A 488 nm argon ion laser was used for FastDiO , whereas
389 a 633 nm He−Ne laser was used for Alexa 647. A 40×1.2 NA water immersion objective was used to
390 focus the light. The fluorescence emission was detected by GaAsP spectral detector in integration
391 mode. The emission detection windows were set as 490 –560 for FastDiO and 650 –700 for AF-647.
392 Intensity traces were recorded for 10 minutes, in total 5 measurements per sample. Curves were then
393 analysed using the python program "Py Profiler", from the reference above.
394 **Serum stability**
395 The stability of the particles in serum (from mice) was tested by measuring the intensity of the
396 fluorescent resonance energy transfer (FRET) pair, DiO/DiI-with whom the particles were labeled. A
397 1:10 mixture of LNPs : mouse serum or LNP:PBS (control) was incubated at 37°C and samples taken
398 at certain timepoints to be measured on a spectrometer (Varioskan). The fluorescence intensity
399 reduction was measured at excitation and emission wavelengths of 480 nm, 530 nm (DiO), and 580 nm
400 (DiI), respectively, to calculate the FRET efficiency. Plots were generated with GraphPad Prism, n=3,
401 mean is shown.
402 **Cryo-TEM imaging of particles**
403 The preparation of LNPs was done immediately before examination and stored in the fridge until the
404 measurements. 4.5ul of a concentrated LNP formulation (lipid concentration 2.3 mg/mL) was placed on
405 a thin carbon-reinforced copper grid for 6 min. The grid was blotted with a filter paper (blot time 4s, blot
406 force 0) to remove the excess of liquid to form a thin film. The samples were vitrified rapidly in liquid
407 ethane at −180 °C. Cryo-TEM measurements were performed using the Glacios TEM from
408 ThermoFisher.
409
410 **Immunological profiling of injected LNPs/LipiGo particles**
411 **Plasma protein analysis**
412 Mouse plasma of particle injected mice was collected after 1h or 48h of injection and stored in -80°C
413 until further analysis with a Thermo Scientific Konelab analyzers to measure the concentration of
414 plasma proteins.
415 **FACS-based cytokine panel analysis**
416 The LegendPlex immune panel (740929, BioLegend) allows for simultaneous quantification of 13 key
417 targets essential for immune response such as IL-4, IL-2, CXCL10 (IP-10), IL-1β, TNF-α, CCL2 (MCP-
418 1), IL-17A, IL-6, IL-10, IFN-γ, IL-12p70, CXCL8 (IL-8), and Free Active TGF-β1.6week old female

419 BALB/c mice were intravenously injected with different formulations (PBS only, std LNP, LipiGo
420 particles) containing 10 µg mRNA/mouse. After 1 h, the blood serum was obtained and used to
421 measure the concentration of pro-inflammatory cytokines using the cytokine panel kit. Mouse Cytokine
422 Panel 2 kit.
423
424 **Protein-corona analysis**
425 Blood serum from wild-type Balb/c mice was collected retro-orbitally (in non-coated microcentrifuge
426 tubes), the blood was left to clot at room temperature for 30 min and then spun down for 15 min at
427 2,000 r.p.m. at 4 °C to retrieve the serum (supernatant). LNPs (50 µl total volume each as described
428 above, encapsulating 1 µg of unlabeled mRNA per formulation) were incubated with mouse serum for
429 15 min at 37 °C at a 1:1 volumetric ratio. A 0.7-M sucrose solution was prepared by dissolving solid
430 sucrose in MilliQ water. The LNP/serum mixture was loaded onto a 300-µl sucrose cushion centrifuged
431 at 15 300g and 4 °C for 1.5 h. The supernatant was removed, and the pellet was washed 3 times with
432 1× PBS, by spinning at 15 300g and 4 °C for 5 min and carefully removing the supernatant. The protein-
433 covered LNPs were then kept dry at −20 °C upon mass spectrometry analysis.
434 To prepare the particles for MS-analysis, they were resuspended in 4% SDS-Tris-HCl buffer (4% SDS,
435 10 mM TCEP, pH 8.5) and incubated at 95 °C for 5 min, followed by sonication for 15 min at 4 °C.
436 Subsequently, 2% SDC buffer (10 mM TCEP, 40 mM CAA) was added, and samples were heated again
437 at 95 °C for 10 min. Proteins were precipitated by adding 3 µl of a 1:1 SpeedBeads mix and ethanol
438 (final concentration 75%) under agitation for 5 min. Beads were immobilized using a magnetic rack,
439 washed twice with 80% ethanol, and dried in a SpeedVac. Samples were digested overnight at 37 °C
440 in 50 µl of 50 mM TEAB containing 0.4 µg Trypsin-LysC and 0.02% LMNG. Peptides were then cleaned
441 using a modified Evotip PURE protocol in a 96-well format, at the end of which they were dried and
442 resuspended in 0.1% TFA containing 0.015% DDM for MS analysis. Finally, peptides (50 ng) were
443 analysed by LC–MS/MS on an EASY-nanoLC 1200 system (Thermo Fisher Scientific) coupled to a
444 timsTOF SCP mass spectrometer (Bruker Daltonik) via a CaptiveSpray ion source. Data were acquired
445 in DIA-PASEF mode with 100 ms ramp and accumulation times. For comparative analysis, 50 ng of
446 peptide was injected onto a 5.5-cm µPAC Neo HPLC column (Thermo Fisher Scientific) and analysed
447 using an 80-min gradient at a flow rate of 250 nl min^{-1}.
448 Data were analyzed using scanpy (v. 1.10.2) and anndata (v. 0.10.8) in Python 3.11. All proteins
449 expressed in less than half of the samples in each group were filtered out, the data was log-transformed
450 and normalized per sample. The missing values were input using KNNImputer (n_neighbors=5) from
451 sklearn package (v. 1.5.1). With scanpy's dendrogram function scipy's hierarchical linkage clustering
452 was calculated on a Pearson correlation matrix over groups which was calculated for 50 averaged
453 principal components. Differential expression analysis was conducted using Scanpy's method
454 `rank_genes_groups` with method set to `t-test`. A threshold of $p < 0.05$ and |log fold change| > 1.0
455 were applied to identify differentially expressed proteins (DEPs). These DEPs were subsequently
456 visualized using volcano plots.
457
458 **Cellular uptake and endosomal escape experiments**

459 HeLa or HeLa-Gal8-mRuby cells were seeded on µ-Slide 18-well glass bottom plates (81817, ibidi) with
460 a density of 10000 or 7000 cells/well 1 day prior to particle exposure. LNP/LipiGo particles were added
461 at an end concentration of 40 nM per well and cells were washed and fixed after 1h/4h or 24h.
462 For samples where lysosome co-staining was desired, AF488-mRNA containing particles were used.
463 HeLa cells were stained with lysotracker DeepRed (L12492, ThermoFisher) at an end concentration of
464 50 nM. 5 min before ending the experiment, cells were stained with Hoechst 33342 (H3570, Invitrogen)
465 at 5ug/ml in PBS 5 min before ending the experiment. Cells were gently washed 3x with warm DPBS
466 to remove excess dyes and then imaged live at an SP5 Leica confocal microscope, image analysis was
467 done with ImageJ.
468 To study uptake in recycling endosomes, Rab11 stainings were conducted in HeLa cells, who were
469 subjected to std LNPs/LipiGo particles. After the incubation of particles with cells, cells were gently
470 washed 3x with DPBS, fixed with 4% PFA-PBS at RT for 10 min and then permeabilized for 5 min with
471 0.1% Triton X-100. Blocking was done with 3% BSA (Carl Roth, 8076.2) for 30 min at RT, after which
472 the cells were stained with 5ug/ml Rab11A-Alexa Fluor 488 (clone 3H18L5, ThermoFisher) (in blocking
473 buffer) at RT for 1h. Dye removal was described as above, before fixing the cells using cold 4% PFA
474 (1176205000, Morphisto) for 10 min at room temperature. Cells were finally washed again (first wash
475 step including Hoechst) and then imaged as described above.
476 To visualize endosomal escape, AF647-mRNA containing particles were incubated with HeLa-mRuby
477 cells, who emit fluorescence at 592 nm upon endosomal rupture. Cells were washed and fixed as
478 described above and then imaged on a confocal microscope. Image representation and "puncta per
479 cell" analysis was done with ImageJ.
480
481 **Aptamer-guided cell-culture targeting of white adipocytes**
482 Standard LNPs and LipiGo(20) particles, decorated with targeting aptamers, were formulated as
483 described above. Cells were seeded in 8-chamber slides (LabTek II) 9 days prior to the experiment.
484 Differention was induced the next day (D0) with induction medium (DMEM, 10% FBS, 1% PenStrep,
485 IBMX-KOH, Indometacin, Dexamethason, T3, Rosiglitazon and Insulin). At D2, medium was chagend
486 to differentiation medium (DMEM, FBS, PenStrep, Rosi, T3, Insulin) and at D5 to differentiation medium
487 without Rosi.
488 40 min before adding the particles ,medium was changed to 130 uL fresh blocking medium (dif. medium
489 containing 100 mg/ L yeast tRNA). 50 ul of the particle solution was added to the wells, so that the
490 resulting concentration of mRNA would be 40 nM in each well. For blank samples, 50 µL of sterile PBS
491 was added to each well. After 40 minutes of particle incubation at 37°C, cells were washed with ice cold
492 PBS before being fixed with 4% PFA for 10min at RT. To quench the crosslinking reaction, cells were
493 incubated 15 min with 0.1 mM Glycine. Unbound particles were then gently washed away 3x with 0.1M
494 DPBS before conducting the staining steps.
495 As pretreatment for the staining, slides were placed 1 min in ice cold 1% Triton-X100-PBS, washed 3x
496 with PBS and then blocked with 1% BSA-PBS at RT for 30 min. Cells were then stained with DAPI
497 (5mg/mL, 1:5000) and Phalloidin (1:200), before being mounted with anti-fade mounting medium and

498 then dried for 2h at RT. Slides were imaged with a SP8 Leica confocal using a 60x objective. Image
499 representation and intracellular dot-based analysis was done with ImageJ.
500
501 ***In vivo* experiments**
502 Female Balb/c mice were obtained from Charles River Laboratories. The animals were housed under
503 a 12-h light/dark cycle and had unlimited access to food and water. The temperature was maintained at
504 18–23 °C, and humidity was at 40–60%. The animals were housed for at least 1 week before entering
505 any experiments. The animal experiments were conducted according to institutional guidelines of the
506 German Mouse Facility at Helmholtz Munich and after approval of the Ethical Review Board of the
507 Government of Upper Bavaria (Regierung von Oberbayern, Munich, Germany) and under European
508 Directive 2010/63/EU for animal research.
509
510 **Tissue clearing of animals (nanoDISCO)**
511 All experiments were performed in triplicates. Mice were deeply anesthetized using a combination of
512 ketamine (70mg/kg) and xylazine (20mg/kg) intraperitoneally. Afterwards, the chest cavity of mice was
513 opened for intracardial perfusion with cold heparinized PBS (10–25 U ml−1 heparin dissolved in 0.01 M
514 PBS) using 100–125-mmHg pressure for 5–10 min at room temperature until the blood was washed
515 out. Next, the mice were perfused with cold 4% paraformaldehyde (PFA) to fix the entire mouse body
516 until stiffness was observed in the tail of the mice. Finally, the skin was carefully removed, and the
517 bodies were fixed in 4% PFA overnight at 4 °C and then transferred to PBS for further processing or
518 directly cleared.
519 The mice were rendered transparent using the nanoDISCO clearing method previously described (Ref
520 Roger paper). In short, mice were placed in a glass chamber and set up in a transcardial circulatory
521 system using peristaltic pumps. After fixation (see above), the mice were intracardially perfused with
522 PBS 3x for 3h, then 2x for 12h with a decolorization solution (1:4 dilution of CUBIC reagent, consisting
523 of 25 wt% N,N,N,N′-tetrakis (2-hydroxypropyl) ethylenediamine (Sigma-Aldrich, 122262) and 15 wt%
524 Triton X-100 (Fisher Scientific, 10287923)). After this, the mouse bodies were washed with PBS for
525 3x4h, and then perfused 2d with a decalcification solution (10 wt/vol% EDTA, pH 8.00). For visualizing
526 a direct signal (such as AF-labeled mRNA), no additional staining was needed and the clearing protocol
527 continued as follows: After another three PBS washes lasting 4h each, the mice were transferred to
528 passive clearing (no transcardial pumping) on a shaker under a hood. We proceeded to incubate the
529 mice in 70 vol% THF (Carl Roth, CP82.1), 90 vol% THF and 2 × 100 vol% THF. This was followed by a
530 20-min treatment with DCM (KK47.1 ,Carl Roth) and finally refractive index matching using BABB (2:1
531 solution containing Benzyl Benzoate (Sigma-Aldrich, W213802) and Benzyl Alcohol(Sigma-Aldrich,
532 1009812500) until the mouse bodies were transparent.
533 For visualizing an mRNA-transcribed EGFP signal, the protocol after the decalcification step continues
534 as follows: After another three PBS washes lasting 4h each, mice were placed in a permeabilization
535 solution containing 35 ul 0.5 g/L signal-enhancing nanobodies(Alexa Fluor 647–conjugated anti-GFP
536 signal-enhancing nanobodies, ChromoTek, gb2AF647). The permeabilization solution (0.5% Triton X-
537 100, 1.5% goat serum (Gibco, 16210072), 0.5 mM methyl-beta-cyclodextrin (Sigma-Aldrich, 332615)

538 and 0.2% trans-1-acetyl-4-hydroxy-L-proline (441562 ,Sigma-Aldrich) was actively pumped
539 transcardially for 5 d at RT and then passively incubated with the mice for an additional 2d. Washing of
540 unbound nanobodies was done with a washing solution (containing 0.5% Triton X-100 and 1.5% goat
541 serum) that was applied 2x12h and 3x4h PBS wash steps. As described above, mice were then
542 passively cleared at room temperature with gentle shaking under a fume hood by incubation in 70 vol%
543 THF, 90 vol% THF, 100 vol% THF and again 100 vol% THF for 12 h each. Then, the mouse bodies were
544 treated with DCM for 20 min and immersed BABB until the tissue was rendered completely transparent.
545
546 **Flow cytometry (FACS)-based immune cell type analysis in animals**
547 All experiments were performed with n=5. 1µg mRNA containing particles (LNPs or LipiGo particles)
548 were intravenously injected into wildtype Balb/c mice and circulated for 1h, before sacrificing the mice
549 via Ketamin/Xylazin overdose, administered intraperitoneally. After administering the anaesthesia,
550 antibodies were injected 3 min prior to perfusion to label intravascular CD45+ cells. Before being
551 perfused with 0.1M PBS, blood was taken from the hearts of the mice from which serum was generated
552 for further analysis. After the perfusion, organs (spleen, liver, lymph node, bone marrow (femur)) were
553 taken from the mice and placed directly into PBS on ice. Mononuclear phagocytes were isolated by
554 enzymatic digestion and density gradient centrifugation, adapted from the reference[27].
555 For processing the liver, organs were transferred into petri dishes for mechanical dissociation with
556 syringe backs until homogenized. The resulting tissue slurry was incubated in digestion buffer
557 containing PBS supplemented with 450 U/mL collagenase I, 125 U/mL collagenase XI, 60 U/mL DNase
558 I, and 60 U/mL hyaluronidase I-S (all from Sigma-Aldrich) at 37 °C for 30 min under agitation. Digested
559 tissues were filtered through a 40 µm cell strainer into 50 mL tubes, followed by centrifugation at 500 g
560 for 7 min at 4 °C. The resulting cell pellets were resuspended in 5 mL of 1× PBS and layered over 5 mL
561 of Histopaque-1077 (Sigma-Aldrich) at room temperature. Samples were centrifuged at 300 g for
562 20 min (acceleration 3, brake 0), and the mononuclear cell layer at the interphase was collected and
563 washed in FACS buffer (Cell Staining Buffer (420201, BioLegend)).
564 Lymph nodes and the spleen were treated with a slightly altered protocol, where the tissue was
565 mechanically dissociated through a 40-µm cell strainer into 20 mL of ice-cold PBS. The cell suspension
566 was pelleted (500 × g, 7 min, 4 °C), washed once with 1 mL of FACS buffer, and centrifuged again.
567 Bone marrow was harvested by removing the femoral epiphyses and flushing the marrow cavity with
568 ice-cold PBS using a 23-gauge needle. The cell suspension was passed through a 40-µm cell strainer,
569 and the cells were pelleted (500 × g, 7 min, 4 °C).
570 After these pretreatments, a common staining step followed, where isolated cells were centrifuged at
571 500 g for 7 min at 4 °C and resuspended in 50–80 µL of FACS buffer (Cell Staining Buffer, 420201,
572 BioLegend). To block Fc receptors, 50 µL of buffer containing 0.5 µL Fc-block (CD16/CD32 Monoclonal
573 Antibody (93), eBioscience™, 14-0161-85, Thermo Fischer) and 0.25 µL Zombie NIR viability dye
574 (BioLegend) was added, followed by incubation for 10 min at RT°C. Subsequently, 50 µL of antibody
575 cocktail was added per tube (antibodies listed below), and samples were incubated for 30 min at 4 °C.
576 Cells were washed with 1 mL FACS buffer and centrifuged again at 500 g for 7 min. Final pellets were

577 resuspended in 250 µL of FACS buffer for acquisition. The cells were measured by a Cytek® Northern
578 Lights™ 3000.
579 The following fluorochrome-conjugated antibodies were used for surface staining: CD3 (clone 17A2,
580 BioLegend), CD45 i.v. (clone 30-F11), CD8a (clone 53-6.7, BD Biosciences), CD11b (clone M1/70,
581 BioLegend), CD35 (clone 8C12, BD Biosciences), CD62L (clone MEL-14, BD Biosciences), CD5 (clone
582 53-7.3, BD Biosciences), B220 (clone RA3-6B2, BioLegend), MHC-II (clone M5/114.15.2, Invitrogen),
583 CD44 (clone IM7, Invitrogen), Ly6G (clone 1A8-Ly6g, Invitrogen), Ly6C (clone AL-21, BD Biosciences),
584 F4/80 (clone BM8, Invitrogen), CD11c (clone N418, Invitrogen), CD45 (clone 30-F11, BioLegend), and
585 CD4 (clone GK1.5, BioLegend). Cell viability was determined using ZombieNIR dye (BioLegend).
586 TX45), anti-MHC-II (FITC, clone M5/114.15.2), anti-Ly6C (PE-eFluor610, clone 1A8-Ly6g), anti-Ly6G
587 (PerCP/Cy5.5, clone HK1.4), anti-F4/80 (PE/Cy7, clone BM8), anti-SIRPα (AlexaFluor700, clone P84),
588 and anti-CD45 (APC/Cy7, clone 30-F11). The antibody mix was generated in the buffer BD Horizon™
589 Brilliant Stain Buffer (566349, BD Biosciences).
590
591 **Bioluminescence imaging**
592 All experiments were performed in triplicates. Mice were injected with LNPs/LipiGo particles
593 encapsulating FLuc-mRNA 24h before imaging. 10 min before imaging the mice were deeply
594 anaesthezized with a Ketamin/Xylazin solution and injected with 150ul of a 15mg/ml aqueous Luciferin
595 solution (VivoGlo luciferin, Promega). intraperitoneally. The animals were then scanned on an IVIS
596 bioluminescent scanner as a whole, before being terminated via cervical dislocation. The organs from
597 the sacrificed mice were then quickly collected for an additional, out-of-body scanning. The exposure
598 time for each scan was set to 60s. The quantifications were assessed of each organ by marking them
599 as individual ROIs to generate the desired values using the Living Image Software version 4.2 (Caliper
600 Life Sciences).
601
602 **Multiphoton imaging for particle Half-Life in blood assessments**
603 Multiphoton imaging was performed using an upright Zeiss LSM710 confocal microscope equipped with
604 a Ti:Sa laser (Coherent, Chameleon Vision II) and two external photomultiplier detectors for red and
605 green fluorescence channels. Eight-week-old C57BL/6N mice (Charles River Laboratories) were
606 anesthetized via intraperitoneal injection of a medetomidine (0.5 mg kg^{-1}), fentanyl (0.05 mg kg^{-1}), and
607 midazolam (5 mg kg^{-1}) mixture (MMF). Body temperature was continuously monitored and maintained
608 using a rectal probe connected to a feedback-controlled heating pad.
609 A catheter was inserted into the femoral artery for administration of fluorescent dyes or nanoparticles.
610 A 4 × 4-mm cranial window was surgically prepared over the right frontoparietal cortex under continuous
611 saline cooling, as previously described. To visualize brain vasculature and acquire baseline images,
612 mice were injected intravenously with FITC-dextran (3 µl g^{-1}). The animal was then positioned on the
613 multiphoton microscope platform, which was adapted for intravital imaging of small animals.
614 Mice was anesthetized, and a rectangular 4x4-mm cranial window was drilled over the right
615 frontoparietal cortex under continuous cooling with saline. After implantation of glass cranial window,
616 mouse was placed under the microscope and the brain vessels were imaged to obtain a baseline.

Afterwards, the nanoparticles labeled with 0.5 mol % FastDIO (0.067ug/kg in a volume of 100 µl.) were systemically injected, and serial imaging was immediately started for at least 2 h. Time-lapse imaging was conducted at an 80-µm tissue depth using 10% laser power at 800 nm. For the FITC channel, a GAASP detector with a long-pass (<570 nm) filter and master gain of 600 was used. The particle channel was recorded using a long-pass (>570 nm) filter and the same master gain setting. Fluorescence signal analysis was performed using ImageJ.

Light-sheet imaging and image visualization of whole cleared mice

Whole-body imaging of cleared mice was performed using a light-sheet fluorescence microscope (Miltenyi Blaze Ultra) equipped with a 4× objective. Mice were mounted ventrally and a z-step size of 6 µm was applied. In the juvenile mice used in this study (<6 weeks of age), a Z-range of 1200–1400 µm was typically sufficient to capture the entire body. To improve sensitivity for detecting nanoparticles, the light-sheet width was reduced to 80%. Scanning was conducted in “light speed mode,” enabling rapid acquisition.

Laser settings were adjusted based on fluorophore characteristics: for 647-labelled mRNA, laser power was set to 100% with an exposure time of 15 s; for background imaging, 80% power and a 5 ms exposure were used. Prior to full dataset transfer, a subset of image tiles was stitched and assessed for image quality to ensure suitability for downstream analysis. Tile stitching was performed on high-performance workstations using a custom Python script. Two-dimensional image stacks were converted to 3D volumes using Imaris Converter, and image visualization, including snapshot generation, was carried out in Imaris Viewer.

SCP-nano particle quantification

The in-house developed SCP-nano pipeline consists of organ segmentation, optional manual organ segmentation correction using VR, and subsequent blob detection, and was described in detail in Luo et al.[15]. In short, for quantifying the particle events per organ, the relative intensity contrast of every segmented LNP dot compared to the background intensity was calculated. The background intensity was estimated per organ by the average intensity of voxels inside the organ while excluding voxels belonging to segmented dots. The relative contrast values of all segmented dots were summed up to reflect the amount of LNP in a specific area or organ. Density heat maps could then be generated based on nanoparticle segmentation to visualize nanoparticle distribution in different organs. A sliding window strategy was employed to compute segmented nanoparticles’ local relative intensity contrast values. A window size of 16 × 16 × 4 voxels was deployed in our experiments. Every voxel in this cube was then assigned with the sum of relative contrast values. Finally, using a 3D Gaussian filter, we obtained a smooth and full-resolution density map.

Immunostaining of tissues and slide scanner imaging

Fixed tissue pieces of perfused mice were dehydrated in a 30% sucrose solution and then sliced in 10 µm slices with a Cryostat and collected on glass slides. 6 slices in per sample were then stained with a classical immunostaining protocol, consisting of 3x 5 min PBS wash, a 15 min permeabilization step

with 0.1% Triton-X100, a 1h blocking step with 3% BSA and an overnight staining step at 4°C with a primary antibody in a buffer containing 0.1% Triton and 3% BSA. Unbound antibody was removed by washing 3x with PBS, before staining with a secondary antibody for 2h at room temperature. Samples were additionally stained with Hoechst (3 min with 7 µM), before being washed 3x with PBS and 1x with ddH_2O. After drying, the mounting medium (VECTASHIELD Antifade, VEC-H-1000, Biozol) was used and slides were closed with cover slips, before being scanned with a slide scanner at the Helmholtz Imaging Core Facility. Automated image analysis was done using the Visiopharm software and plots generated with GraphPad Prism.

References

1 He, Y., Wang, Y., Wang, L., Jiang, W. & Wilhelm, S. Understanding nanoparticle-liver interactions in nanomedicine. *Expert opinion on drug delivery* **21**, 829-843 (2024).

2 Hosseini-Kharat, M., Bremmell, K. E. & Prestidge, C. A. Why do lipid nanoparticles target the liver? Understanding of biodistribution and liver-specific tropism. *Molecular Therapy Methods & Clinical Development* **33** (2025).

3 Dilliard, S. A. & Siegwart, D. J. Passive, active and endogenous organ-targeted lipid and polymer nanoparticles for delivery of genetic drugs. *Nature Reviews Materials* **8**, 282-300 (2023).

4 Cheng, Q. *et al.* Selective organ targeting (SORT) nanoparticles for tissue-specific mRNA delivery and CRISPR–Cas gene editing. *Nature nanotechnology* **15**, 313-320 (2020).

5 Rurik, J. G. *et al.* CAR T cells produced in vivo to treat cardiac injury. *Science* **375**, 91-96 (2022).

6 Tarab-Ravski, D. *et al.* Delivery of therapeutic RNA to the bone marrow in multiple myeloma using CD38-targeted lipid nanoparticles. *Advanced Science* **10**, 2301377 (2023).

7 Grzetic, D. J., Hamilton, N. B. & Shelley, J. C. Coarse-grained simulation of mRNA-loaded lipid nanoparticle self-assembly. *Molecular Pharmaceutics* **21**, 4747-4753 (2024).

8 Albertsen, C. H. *et al.* The role of lipid components in lipid nanoparticles for vaccines and gene therapy. *Advanced drug delivery reviews* **188**, 114416 (2022).

9 Wilson, S. C. *et al.* Real time measurement of PEG shedding from lipid nanoparticles in serum via NMR spectroscopy. *Molecular Pharmaceutics* **12**, 386-392 (2015).

10 Barbier, A. J., Jiang, A. Y., Zhang, P., Wooster, R. & Anderson, D. G. The clinical progress of mRNA vaccines and immunotherapies. *Nature biotechnology* **40**, 840-854 (2022).

11 Cheng, Q. *et al.* Dendrimer-based lipid nanoparticles deliver therapeutic FAH mRNA to normalize liver function and extend survival in a mouse model of hepatorenal tyrosinemia type I. *Advanced materials* **30**, 1805308 (2018).

12 Zaleski, M. H. *et al.* Conjugation chemistry markedly impacts toxicity and biodistribution of targeted nanoparticles, mediated by complement activation. *Advanced Materials* **37**, 2409945 (2025).

13 Yazdi, M. *et al.* In Vivo Endothelial Cell Gene Silencing by siRNA-LNPs Tuned with Lipoamino Bundle Chemical and Ligand Targeting. *Small* **20**, 2400643 (2024).

14 Mui, B. L. *et al.* Influence of polyethylene glycol lipid desorption rates on pharmacokinetics and pharmacodynamics of siRNA lipid nanoparticles. *Molecular Therapy Nucleic Acids* **2** (2013).

15 Luo, J. *et al.* Nanocarrier imaging at single-cell resolution across entire mouse bodies with deep learning. *Nature Biotechnology*, 1-14 (2025).

16 Pohar, J., Kužnik Krajnik, A., Jerala, R. & Benčina, M. Minimal sequence requirements for oligodeoxyribonucleotides activating human TLR9. *The Journal of Immunology* **194**, 3901-3908 (2015).

17 Campbell, J. D. Development of the CpG adjuvant 1018: a case study. *Vaccine adjuvants: methods and protocols*, 15-27 (2016).

18 Yoshida, T. *et al.* Introduction of sugar-modified nucleotides into CpG-containing antisense oligonucleotides inhibits TLR9 activation. *Scientific Reports* **14**, 11540 (2024).

19 Voke, E. *et al.* Protein corona formed on lipid nanoparticles compromises delivery efficiency of mRNA cargo. *bioRxiv*, 2025.2001. 2020.633942 (2025).

20 Swingle, K. L. *et al.* Placenta-tropic VEGF mRNA lipid nanoparticles ameliorate murine pre-eclampsia. *Nature* **637**, 412-421 (2025).
21 Zhang, R. *et al.* Helper lipid structure influences protein adsorption and delivery of lipid nanoparticles to spleen and liver. *Biomaterials science* **9**, 1449-1463 (2021).
22 Chen, D., Parayath, N., Ganesh, S., Wang, W. & Amiji, M. The role of apolipoprotein-and vitronectin-enriched protein corona on lipid nanoparticles for in vivo targeted delivery and transfection of oligonucleotides in murine tumor models. *Nanoscale* **11**, 18806-18824 (2019).
23 Davis, S. *et al.* Isolation of angiopoietin-1, a ligand for the TIE2 receptor, by secretion-trap expression cloning. *Cell* **87**, 1161-1169 (1996).
24 Ussar, S. *et al.* ASC-1, PAT2, and P2RX5 are cell surface markers for white, beige, and brown adipocytes. *Science translational medicine* **6**, 247ra103-247ra103 (2014).
25 Engelen, W., Meijer, L. H., Somers, B., De Greef, T. F. & Merkx, M. Antibody-controlled actuation of DNA-based molecular circuits. *Nature Communications* **8**, 14473 (2017).
26 Sych, T. *et al.* High-throughput measurement of the content and properties of nano-sized bioparticles with single-particle profiler. *Nature biotechnology* **42**, 587-590 (2024).
27 Simats, A. *et al.* Innate immune memory after brain injury drives inflammatory cardiac dysfunction. *Cell* **187**, 4637-4655. e4626 (2024).

Acknowledgements
This work was supported by the European Research Council Consolidator grant (no. GA 865323), Nomis Heart Atlas project grant (Nomis Foundation) and Helmholtz Association Program Helmholtz IVF, ZT-I-PF-4-091, FOMIA. S.H. was funded by the Amgen Scholarship program. Additionally, we would like to thank Prof. J. Cui for the access to dynamic light scattering measurements, the Helmholtz Core facility for electron microscopy (Dr. Carsten Peters) for the guidance with the Cryo TEM images, the group of Prof. Ernst Wagner for providing HeLa-Gal8-mRuby3 cells for the endosomal escape assays, Dr. David Jürgens for running the Cytokine Assay, the Helmholtz Core Facility Imaging (Dr. Annette Feuchtinger) for helping us with the Slide Scanner imaging and analysis, as well as Dr. Doris Kaltenecker for serum protein analysis.

Competing Interest Statement
K.Kadletz, C.Kimna and A.Ertürk have filed for intellectual property on the hybrid nanoparticles described herein. A.Ertürk. is a co-founder of Deep Piction. The other authors declare no competing interests.

Authors and Affiliations

Institute for Intelligent Biotechnologies (iBIO), Helmholtz Center Munich, Neuherberg, Germany
Karoline Kadletz, Ceren Kimna, Denise Jeridi, Sofia Hu, Jakub Grzejdak, Izabela Horvath, David-Paul Minde, Mayar Ali, Luciano Höher, Eren Aydeniz, Yagmur Ayse Kulcu, Farida Hellal, Markus Elsner, Ali Erturk

Institute for Stroke and Dementia Research, Klinikum der Universität München, Ludwig-Maximilians University Munich, Munich, Germany
Ceren Kimna, Olga Carofiglio, Igor Khalin, Ying Chen, Alessio Ricci, Arthur Liesz, Farida Hellal, Ali Ertürk

Munich Cluster for Systems Neurology (SyNergy), Munich, Germany
Karoline Kadletz, Ceren Kimna, Olga Carofiglio, Igor Khalin, Ying Chen, Izabela Horvath, Alessio Ricci, Arthur Liesz, Farida Hellal, Ali Erturk

Deep Piction, Munich, Germany
Karoline Kadletz, Ceren Kimna, Denise Jeridi, Izabela Horvath, Markus Elsner, Ali Ertürk

Faculty of Medicine, Ludwig-Maximilians University Munich, Munich, Germany
Ying Chen

TUM School of Computation, Information and Technology, Technical University of Munich, Munich, Germany
Izabela Horvath

Research Unit Adipocytes & Metabolism (ADM), Helmholtz Diabetes Center, Helmholtz Zentrum München, Neuherberg, Germany
Valentin Kenneth Reichenbach, Siegfried Ussar

German Center for Diabetes Research (DZD), Neuherberg, Germany
Valentin Kenneth Reichenbach, Siegfried Ussar

Graduate School of Neuroscience (GSN), Munich, Germany
Mayar Ali

Institute of Computational Biology, Helmholtz Munich, Neuherberg, Germany
Mayar Ali

Normandie University, UNICAEN, INSERM UMR-S U1237, Physiopathology and Imaging of Neurological Disorders (PhIND), GIP Cyceron, Institute Blood and Brain @Caen-Normandie (BB@C), Caen, France
Igor Khalin

Science for Life Laboratory, Department of Women's and Children's Health, Karolinska Institutet, Solna, Sweden
Taras Sych, Erdinc Sezgin

School of Medicine, Koç University, İstanbul, Turkey
Ali Erturk

Contributions

A.E. conceived the project as a whole, including the sections on particle design, imaging and AI analysis. K.K. conducted the particle design, K.K. and C.K conducted all experiments involving particle production and characterization, light-sheet imaging and analysis. I.H. worked on the organ segmentation, L.H. and E.A. conducted corrections using VR tools. A.L conceptualized and O.C. and A.C. conducted the experiments on immune cell analysis with FACS. K.K. and S.H. planned and S.H. executed experiments involving aptamer decoration of particles. J.G. worked on immunohistology analysis of the particles in tissues. C.K. and K.K conducted protein corona experiments, D.-P.M. performed proteomics sample preparation and mass spectrometry and M.A. conducted the proteomics analysis. S.U. and V.K.R. designed and V.K.R. conducted the adipocyte cell culture experiments. D.Jeridi. conducted all i.v. particle injections and helped with the immunology FACS experiments, clearing and imaging. Y.A.K. contributed to tissue clearing and imaging. I.K. planned and executed experiments involving intravitreal imaging. T.S. and E.S. helped set up and analyze experiments on SPP analysis of the particles. A.E., M.E. and F.H. provided overall supervision for the project. K.K. and C.K. wrote the manuscript; C.K. and M.E. revised the text, F.H. revised the figures.

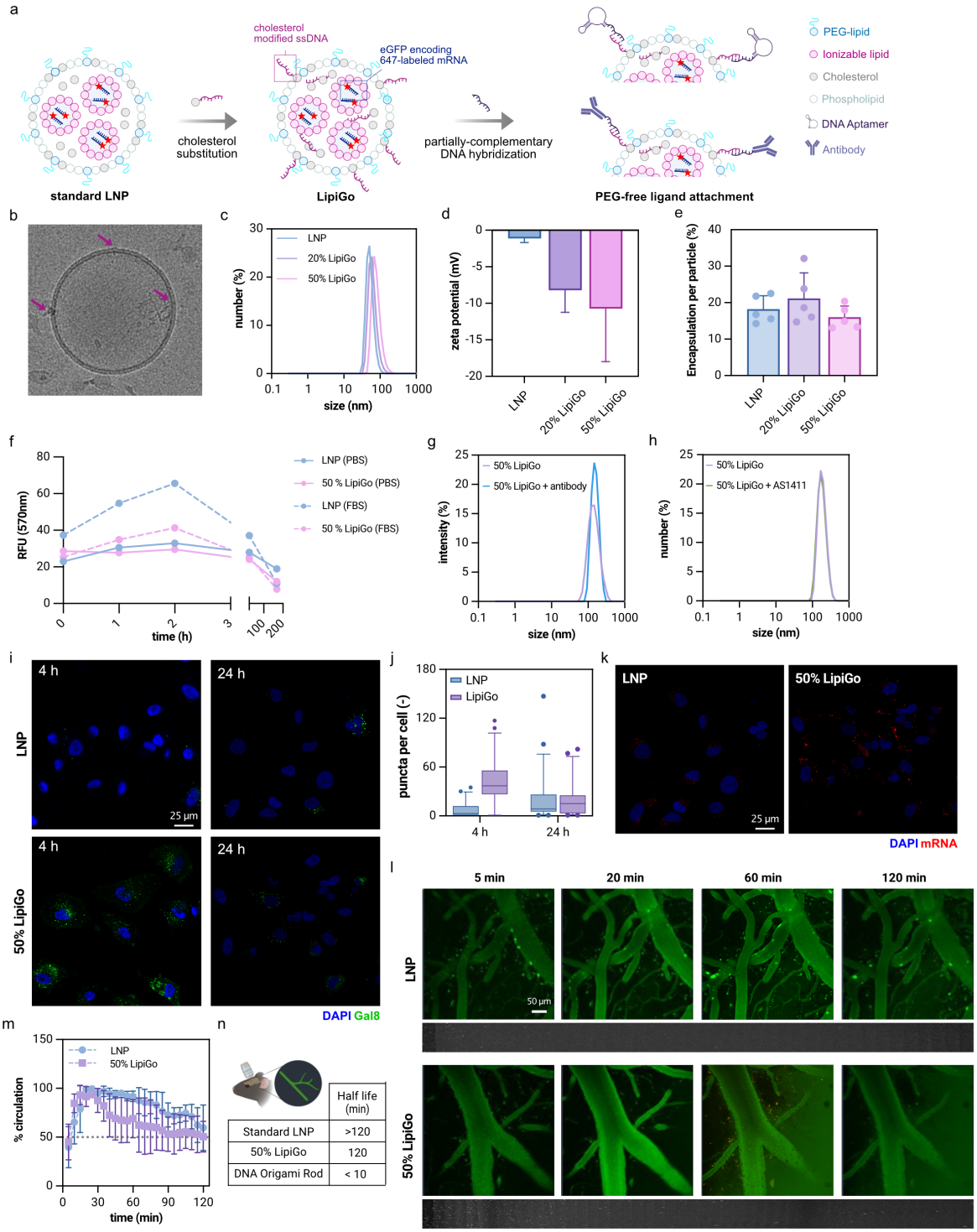

Fig. 1. Design and characterization of LipiGo nanoparticles. a) Schematic of LipiGo design. Partial substitution of cholesterol with cholesterol-modified ssDNA enables ligand attachment via complementary base pairing. **b)** Representative Cryo-TEM image of LipiGo particle showing protruding DNA strands (arrows). **c)** Hydrodynamic size distribution of standard LNPs and LipiGo variants measured with DLS. **d)** Zeta potential measurements showing increased negative sharge with higher DNA substitution (N=5). **e)** mRNA encapsulation efficiency of LNPs and LipiGo variants (N=5). **f)** Stability of LNPs and LipiGo particles measured in PBS and serum supplemented media measured with FRET. **g,h)** Hydrodynamic size distribution of LipiGo before and after hybridization with IgG antibody (g) or AS1411 DNA aptamer (h). **i)** Representative confocal images of Gal8 recruitment assay in HeLa cells shows enhanced endosomal rupture at 4 h with LipiGo compared to LNPs. **j)** Quantification of Gal9 puncta per cell (N = 50 cell per condition**). k)** Representative confocal images of HeLa cells after 24 h incubation with LNP or LipiGo particles**. l)** Intravital two-photon microscopy images of LNPs and LipiGo in mouse vasculature at indicated time points. **m)** Quantification of circulation profiles showing slightly

shorter half-life of LipiGo compared to standard LNPs. **n)** Summary of measured circulation half-lives comparing standard LNPs, LipiGo particles, and DNA origami particles[15].

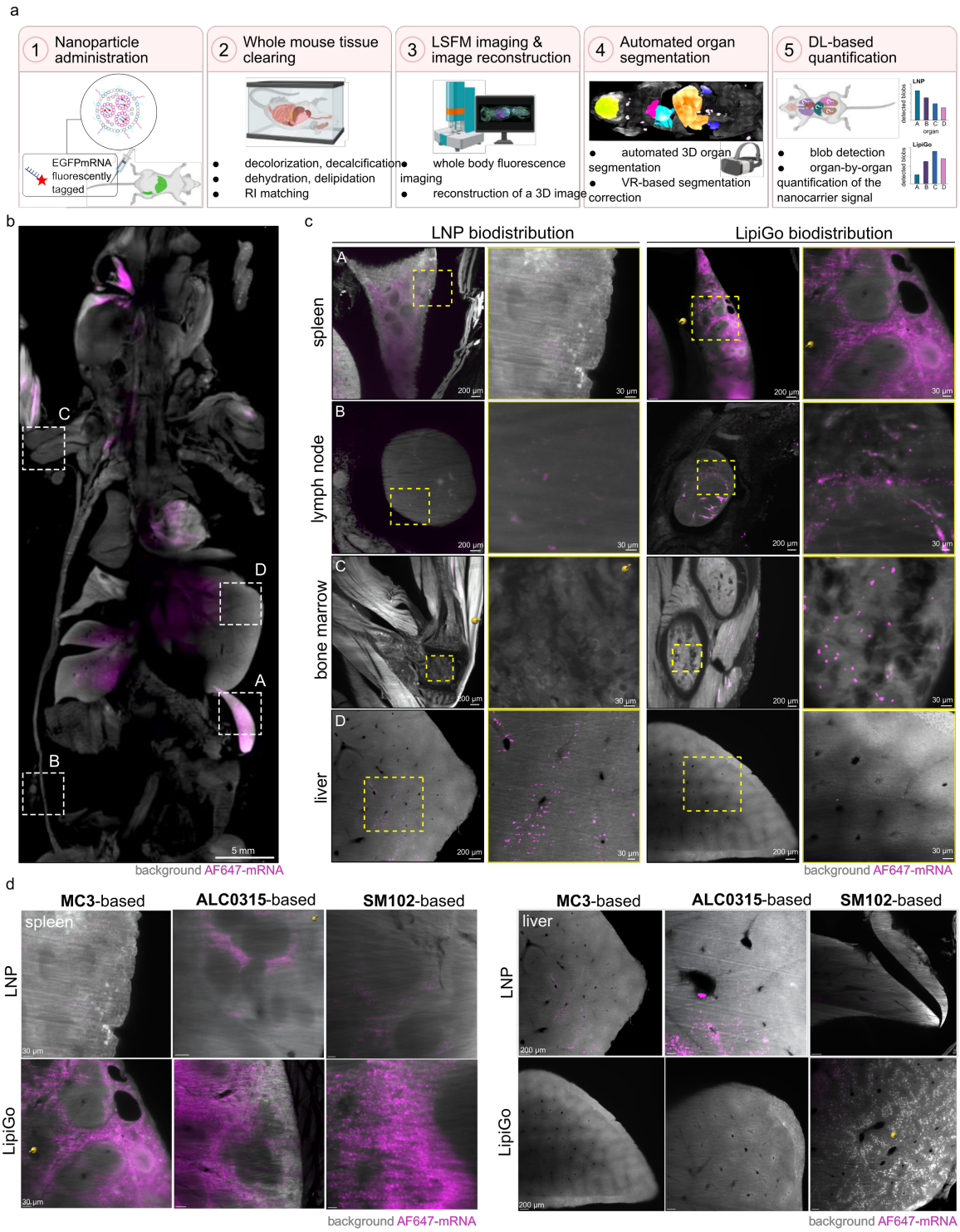

Fig. 2. Whole-body mRNA biodistribution assessment of LipiGo particles assessed by SCP-Nano. a) Schematic of the SCP-nano workflow: (1) fluorescently labelled mRNA-loaded nanoparticle administration, (2) whole body tissue clearing, (3) light-sheet fluorescence microscopy (LSFM) imaging and 3D reconstruction, (4) automated organ segmentation with manual refinement, and (5) deep learning-based signal quantification. **b)** Whole-body 3D projection (600 µm slice) of a mouse 1 h after i.v. injection of LipiGo. **c)** Representative LSFM images of spleen, lymph node, bone marrow and liver, comparing biodistribution of standard LNPs and LipiGo formulations. Yellow dashed boxes indicate regions of interest (ROI) with close-up views, with particularly

enhanced accumulation in immune organs for LipiGo. **d)** Comparison of spleen and liver biodistribution of nanoparticles formed with different base ionizable lipids (MC3, ALC0315, and SM-102), showing consistent spleen targeting across LipiGo variants.

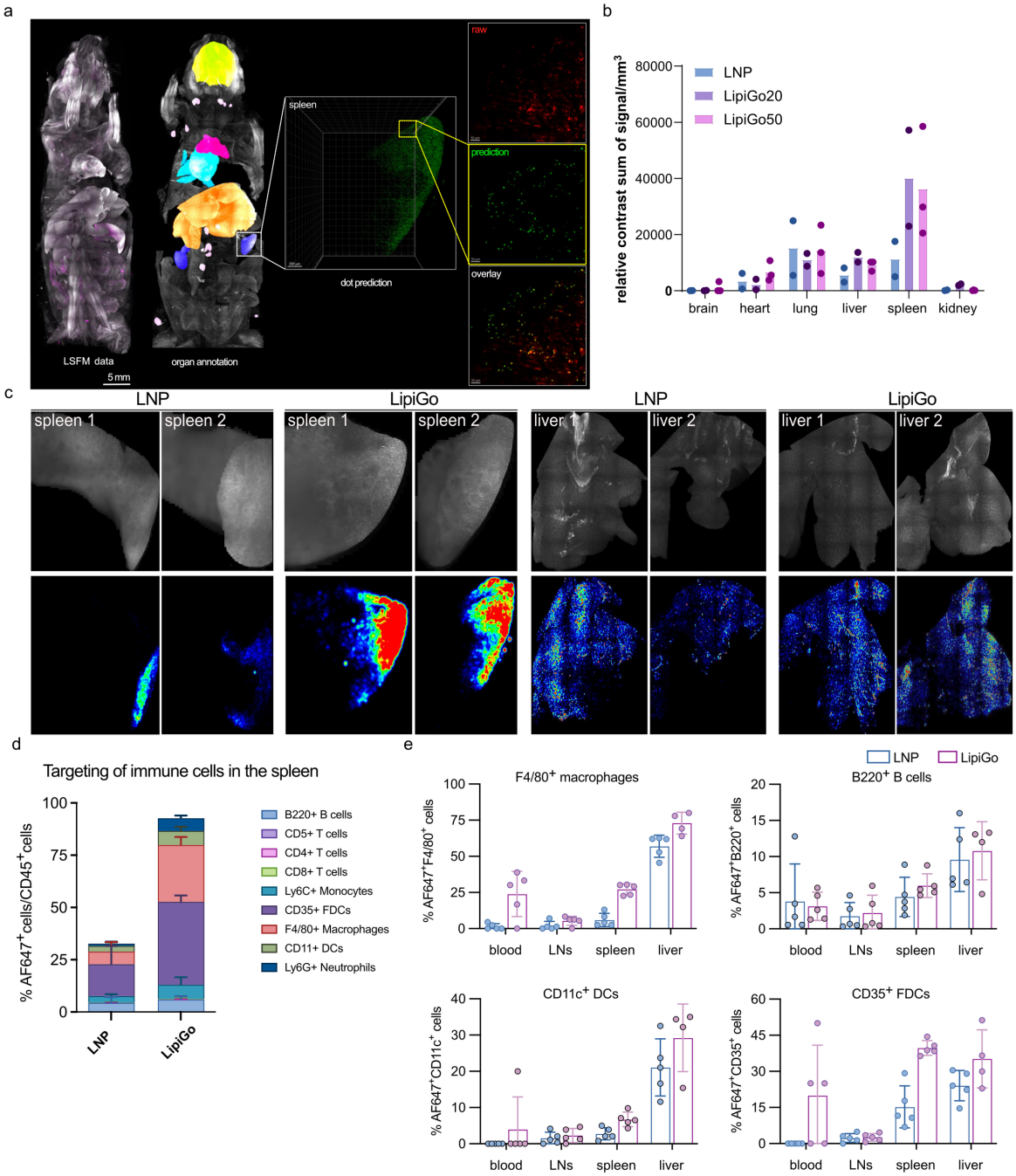

Fig. 3. Quantitative profiling of LipiGo biodistribution at the organ and immune cell level. a) Light sheet fluorescence microscopy (LSFM)-based whole-body analysis workflow showing automated organ segmentation and nanoparticle signal prediction. Representative spleen region from a LipiGo-injected mouse is shown as raw (red), predicted (green), and overlay images. **b)** Quantification of relative nanoparticle accumulation across major organs 1 h post administration using SCP-nano analysis (N = 3). **c)** Representative SCP-nano quantified particle distribution density heatmaps for spleen and liver (N=2). **d)** Flow cytometry analysis of immune cells subtypes in the spleen (CD45$^+$ cells) showing the percentage of LNP (mRNA-AF647$^+$) positive cells in the respective immune cell populations (N=5). **e)** Quantification of AF647$^+$ cells among F4/80$^+$ macrophages, B220$^+$ B cells, CD11c$^+$ dendritic cells (DCs) and CD35$^+$ follicular dendritic cells (FDCs) in blood, lymph nodes (LNs), spleen, and liver (N=5). Data are shown as mean ± SD.

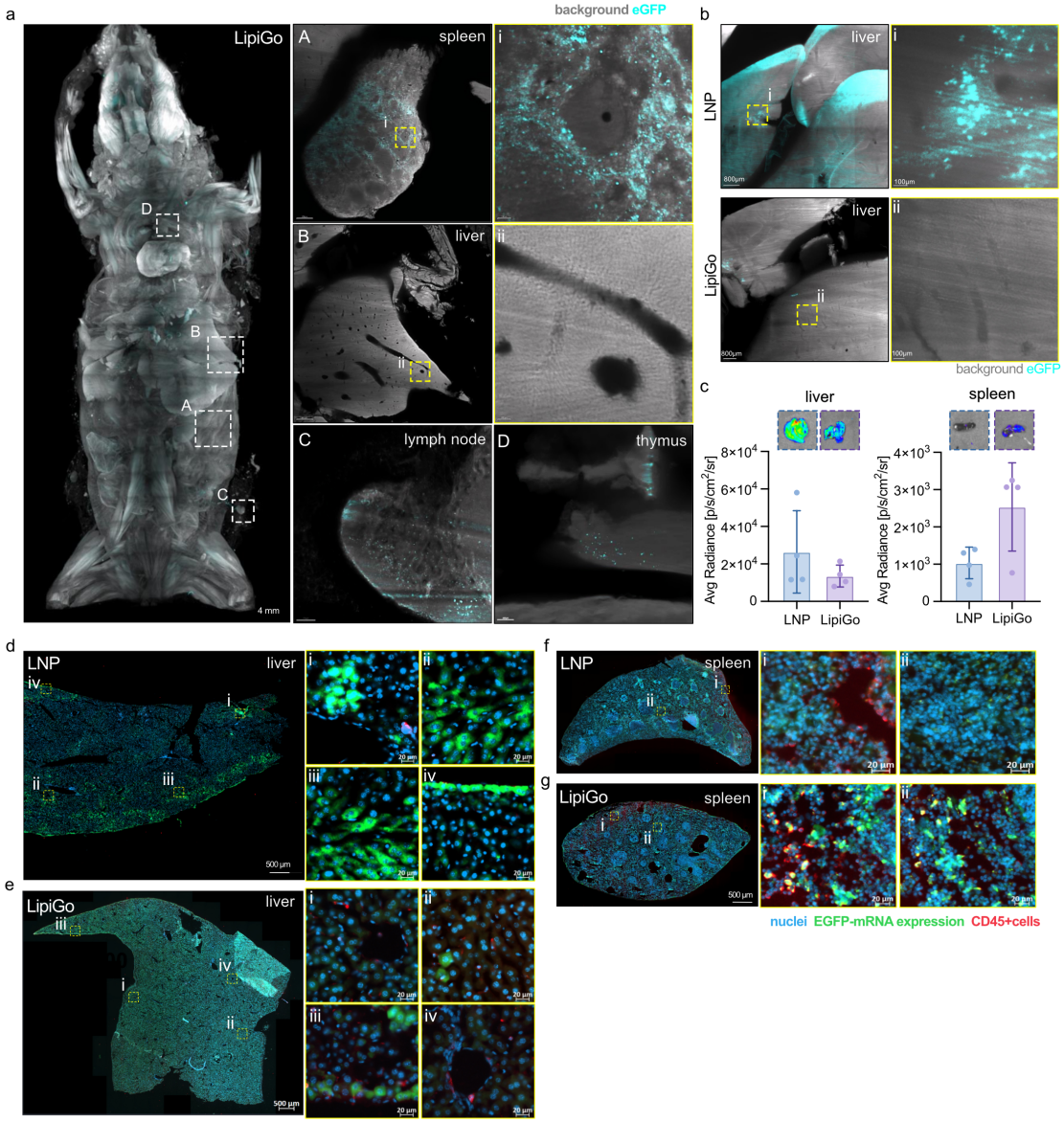

Fig. 4. LipiGo enables functional mRNA delivery to immune cell rich organs. a) Whole-body 3D projection (600 µm) of a mouse 48 h post i.v. injection of LipiGo delivering EGFP mRNA. Dashed boxes indicate ROIs in the spleen, liver, lymph node and thymus. **b)** EGFP expression in livers of mice treated with standard LNPs or LipiGo, demonstrating reduced hepatic expression with LipiGo. **c)** Bioluminescence imaging and quantification of FLuc mRNA expression in liver and spleen 24 h post-injection of standard LNP and LipiGo (N=3). **d-g)** Immunofluorescence staining of fresh frozen tissue sections of liver (d,e) and spleen (f,g) (10 µm) showing EGFP expression (green), DAPI nuclear staining (blue), and CD45^{+} immune cells (red).

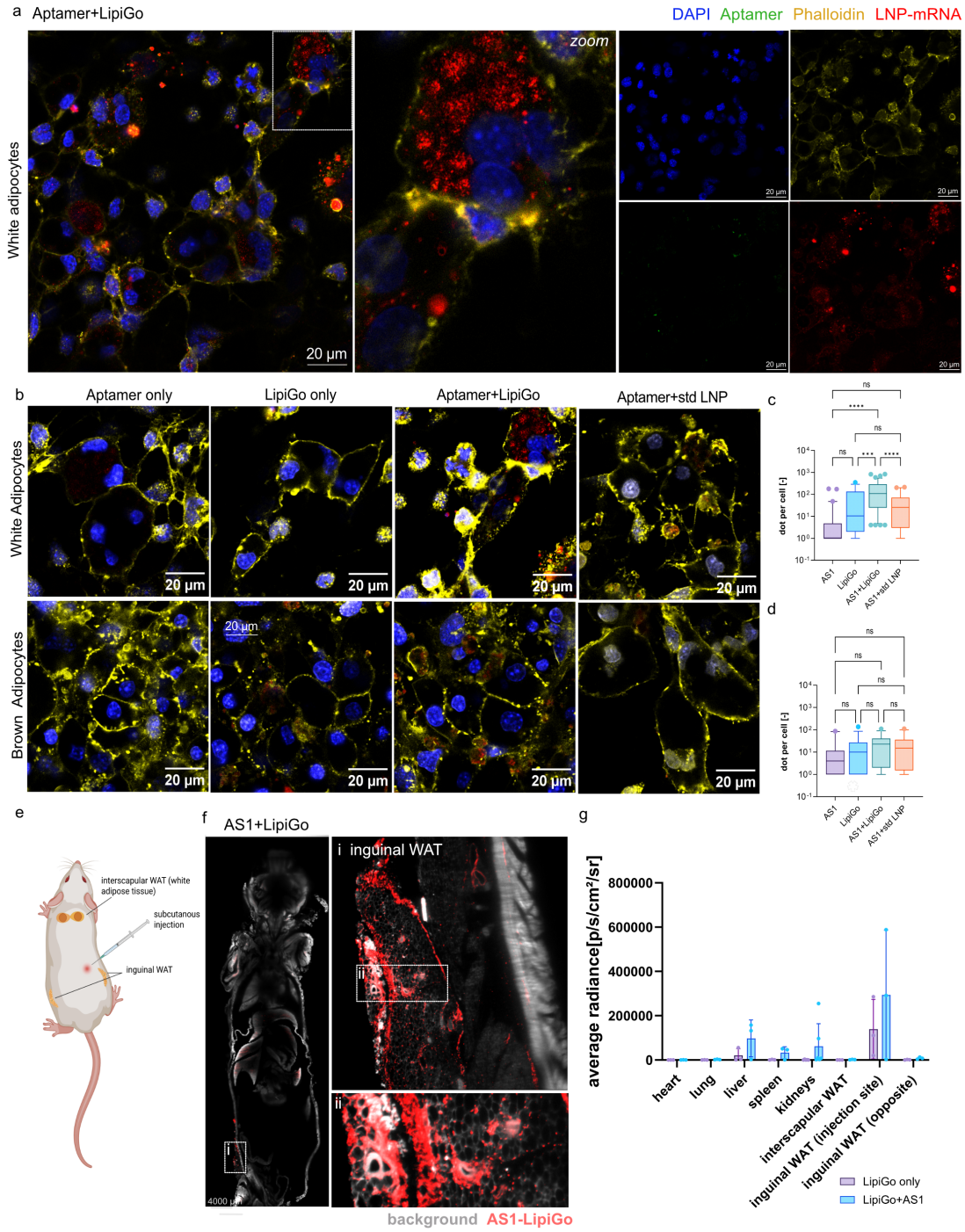

Fig 5: Specific targeting and functional mRNA delivery to white adipocytes *in vitro* and *in vivo*. a) Representative confocal microscopy image of differentiated white adipocytes after incubation with LipiGo particles conjugated with the Asc1-surface protein-targeting aptamer (AS1-LipiGo). The particles encapsulate labeled mRNA (red) and are functionalized with a FAM-labeled aptamer (green). The image shows significant internalization and co-localization of both components within intracellular compartments. Cell nuclei are stained with DAPI (blue). **b.** *In vitro* specificity assessment. The top row shows white adipocytes incubated with control formulations: non-conjugated AS1 aptamer, untargeted LipiGo, and standard LNPs lacking the DNA handle but unspecifically mixed with AS1. Only the fully conjugated AS1-LipiGo particles show significant uptake. The bottom row shows the same set of experiments performed on brown adipocytes, which lack the insulin receptor. **c-d.** Quantification of the mRNA signal inside the white (c) and brown (d) adipocytes. One-way ANOVA with Tukey's multiple comparison test with a single pooled variance is employed. **e.** Schematic overview of the *in vivo* study design. Mice were subcutaneously (s.c.) injected with either AS1-LipiGo or untargeted LipiGo particles, to evaluate targeted delivery and functional protein expression. **f.** Whole body imaging of a tissue cleared mouse showing the biodistribution of AS1-LipiGo after 1 h circulation (left) with a zoom in to inguinal

WAT (right). **g.** *Ex vivo* quantification of functional mRNA delivery. Bioluminescence signal from luciferase expression was measured in harvested organs 24 hours post-injection. The quantification reveals that AS1-LipiGo particles (**d**) mediate significantly higher luciferase expression in the target inguinal white adipose tissue (WAT) compared to the untargeted LipiGo control particles (**e**), with minimal off-target expression observed in other organs. Data are presented as mean ± s.d. (n=3 mice per group).